



Contents lists available at ScienceDirect

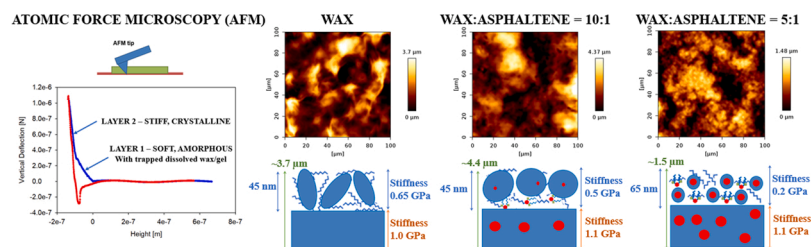
Colloids and Surfaces A: Physicochemical and Engineering Aspects

journal homepage: www.elsevier.com/locate/colsurfa

Alterations in paraffin wax crystal networks induced by asphaltenes and pour point depressants, investigated by atomic force microscopy

George Claudiu Savulescu^{a,*}, Maja Rücker^b, Sébastien Simon^a, Gisle Øye^a^a Ugelstad Laboratory, Department of Chemical Engineering, Norwegian University of Science and Technology (NTNU), Trondheim N-7491, Norway^b Energy Technology, Department of Mechanical Engineering, Eindhoven University of Technology, Eindhoven, MB 5600, Netherlands

GRAPHICAL ABSTRACT



ARTICLE INFO

Keywords:

Atomic force microscopy
Wax
Stiffness
Crystallinity
Young Modulus
Surface forces

ABSTRACT

Wax crystallization in pipelines in cold environments is a key factor affecting flow assurance during crude oil production. Polar crude oil components, such as asphaltenes, and polymeric pour point depressants (PPDs) have been demonstrated to interact with wax during gelation and crystallization through complex formation during nucleation or crystal growth alteration which leads to co-crystallization. This study introduces a methodology based on atomic force microscopy (AFM) to characterize features of solid surfaces precipitated from model wax, wax-PPD, wax-asphaltene and asphaltene systems. Height data collected from AFM measurements enabled the quantification of modifications in crystal sizes and shapes induced by the presence of asphaltenes and PPDs. The 2D Fourier transform of the height was used to generate statistics for the frequency of height amplitude, revealing information about the pore size and the height patterns. A stiffness/elasticity analysis was used to calculate the Young Modulus of the upper layers. In wax and wax-asphaltene systems, two nano-scale layers with different Young Modulus profiles emerged. The nano-scale layer on the top was softer and corresponded to more amorphous wax crystal networks with trapped dissolved wax. The nano-scale layer on the bottom was stiffer, comprising of more crystalline structures, corresponding to wax crystals with lower deviations from full crystallinity, with properties independent of asphaltene concentration. A bilayer did not form in the presence of PPD, which prevented the formation of amorphous phases with trapped dissolved wax or gel. After a methodology for model systems was established, the focus moved to systems based on production wax i.e. recovered from deposits. This was complemented by a comparison between model precipitation conditions and precipitation by cold finger, resembling industrial processes. Results highlighted the effect of change in chemical composition on topography, elasticity and adhesion of the surface. AFM provided new insights into wax crystallization patterns in the presence of inhibitors, which can be used to quantify the extent of wax-inhibitor interactions and project it

* Corresponding author.

E-mail address: g.savulescu@tue.nl (G.C. Savulescu).<https://doi.org/10.1016/j.colsurfa.2024.133843>

Received 24 January 2024; Received in revised form 13 March 2024; Accepted 29 March 2024

Available online 30 March 2024

0927-7757/© 2024 The Author(s). Published by Elsevier B.V. This is an open access article under the CC BY license (<http://creativecommons.org/licenses/by/4.0/>).

on production systems. The method could be used to explain macro-scale rheological properties of oils during flow assurance in the future.

1. Introduction

Paraffin waxes are *n*-, iso- or cyclo- alkanes, with a number of carbons between 18 and 100, or sometimes higher [1]. Crude oils contain waxes in variable concentrations, usually dependent on the extraction field. Wax precipitates when the crude oils are cooled below the wax appearance temperature (WAT), which is specific to each oil. Wax crystallization processes are often followed by gelation and deposition, which can result in operability issues, negatively affecting flow assurance. One of the most affected properties is the pour point, which is defined as the temperature at which the oil cannot flow anymore. Common effects of the increased fluid viscosity and alterations in the reservoir fluid include a decrease in the oil flow in the pipeline, pressure abnormalities, pipeline restart problems and in the worst case a complete blockage of the flow [2].

A conventional method to decrease the wax appearance temperature and especially the pour point below the desired operating temperatures, is the use of polymeric pour point depressants, which act as wax crystallization modifiers [3]. PPDs manifest high affinity for the non-polar moieties of wax, which leads to complex formation during the gelation phase of wax crystallization [4,5]. Without the PPD, wax often grows predominantly in 2 dimensions, through the parallel alignment of long alkane chains [6,7]. The result is the formation of needle, rod or plate-like crystals. The PPD prevents interaction between parallel long alkane chains and promotes growth in 3 dimensions. Therefore, wax-PPD complexes have a different crystallization mechanism, which leads to rounder, more dendritic crystals [4,5,8]. The consequences of these phenomena are a lowered wax appearance temperature, higher solubility and altered crystal features, such as lower aspect ratio and surface area, reducing the negative effects of wax deposition [4,5].

Asphaltenes are crude oil components with a complex chemical structure. They consist of various polycyclic aromatic hydrocarbons and aliphatic chains, containing heteroatoms, such as nitrogen, oxygen or sulfur and metals such as nickel, vanadium and iron [2]. They contain a non-polar part and a polar part, the former of which has also been demonstrated to interact with wax during crystallization [9]. At low concentrations, asphaltenes are present as dissolved monomers in toluene or other aromatic solvents. However, when the asphaltene concentration is high enough, nanoaggregates (2–5 nm in diameter) and nanoclusters (>5 nm in diameter) can form, at a concentration point often referred to as critical nanoaggregate concentration (C.N.A.C) [10, 11]. These nanoaggregates and nanoclusters are believed to interfere with wax during the early stages of crystallization [11,12]. Their larger size facilitates their behavior as nucleation sites for wax, promoting the formation of more finely dispersed, smaller wax-asphaltene co-crystals. The non-polar groups of asphaltene molecules can also have a separate effect on wax crystallization. As wax molecules are also non-polar, these groups are expected to behave as binders between the wax crystals during the crystal growth phase of crystallization [12–14]. The result is the distortion of wax crystals which cannot grow as large as in the absence of asphaltenes. Moreover, crystal growth by parallel alignment of alkane chains is spatially hindered by the asphaltenes acting as binders. Therefore, the needle shape is not achieved anymore. Instead, rounder, dendritic crystals are formed. These phenomena also affect the gelation process, which weakens the crystal network and reduce the gel strength [9,12,13]. Although the modified wax-asphaltene co-crystals allow for better crude oil flow, they might increase WAT and the wax precipitation rate [13,15–18]. Moreover, unlike PPDs, asphaltenes could also precipitate independently of wax, interfering with concurrent wax crystallization, by inducing steric effects which affect wax nucleation and crystal growth.

The wax-inhibitor interactions were recently analyzed in literature. The main focus was the investigation of molecular mobility and wax precipitation rate by analyzing wax crystallization using toluene as a solvent. Savulescu et al. introduced several NMR techniques for this purpose [8,19]. Their studies quantified and proved co-crystallization [20]. The evolution of asphaltene-specific liquid signal with temperature showed that asphaltene content decreased by 30% more from 30 °C to 0 °C, when wax was present. A separate NMR study [21] has indicated a loss in the mobility of asphaltenes, when wax started crystallization, which demonstrated that asphaltenes got trapped in the wax crystalline matrix, co-crystallizing. Moreover, the NMR studies found that a threshold asphaltene concentration, associated with complete self-association to nanoaggregates and nanoclusters, generated an increase in the amount of precipitated wax and in the amount of low mobility dissolved wax trapped inside the newly formed wax crystal network during crystallization. The possible mechanisms which led to the wax trapping process and to the intensification of trapping in the presence of asphaltenes were previously proposed by Savulescu et al. [8]. The first was the formation of wider gaps in the crystal network induced by the altered geometry of the packing in wax-asphaltene co-crystal networks. The second was the formation of smaller pores in the smaller wax-asphaltene co-crystals, which had a higher tendency to reduce the mobility of dissolved wax and consequently trapped a higher amount of dissolved wax. The third was the formation of an outer layer consisting of softer, more amorphous wax and wax-asphaltene phases, which favored the trapping of a higher amount of wax. This wax was likely attracted or bound to the crystal network surface. NMR could only assess bulk and surface phenomena corresponding to the fluid mobility in the bulk or at the solid-liquid interface. This study will introduce atomic force microscopy as an alternative to characterize properties corresponding to the solid phase (height, stiffness, adhesion force).

To assess alterations in solid wax networks, methods such as cross polarized microscopy and scanning electron microscopy have also been used before to generate images of wax crystal networks in absence and in presence of asphaltenes and PPDs [22,23]. Smaller, more compact crystals were identified in presence of PPD by both CPM (cross polarized microscopy) and SEM. A transition from a plate-like shape to spherical shape was also noticed with SEM. For asphaltenes, only CPM was used, demonstrating smaller crystals [23]. Although promising, these results do not fully explain the wax crystallization mechanism and it particularly does not explain the effect of asphaltene concentration. Moreover, SEM does not allow to characterize the stiffness or level of crystallinity of layers on the surface. The SEM scan is a 2D scan and a 3D image could only be obtained by merging 2D slices, which decreases accuracy. This study will overcome these limitations by introducing atomic force microscopy as an alternative to analyze wax and wax-inhibitor systems.

Although many hypotheses were expressed, the exact mechanism behind the impact of inhibitors on wax precipitation is not clear. This study aims to introduce an AFM-based method to assess the level of alteration which is caused by inhibitors to the wax crystal network. To investigate a potential change in the stiffness/elasticity of wax and wax-inhibitor networks, AFM was proposed as a technique to characterize the elasticity of the resulting crystal networks. The focus was placed on solid crystal networks, in which the final consequences of crystal network alterations could also be observed by AFM from a topographic point of view (i.e. crystal size, surface patterns). The novelty of the AFM-based technique was also complemented by nano-scale resolution in 3D for scanning the crystal layers. For this purpose, height, 2D Fast Fourier Transform of the height, Young Modulus and adhesion data were determined.

The first focus of the article was to investigate the effect of PPD and

asphaltene on model wax crystal networks, by characterizing model wax, wax-asphaltene and wax-PPD crystal networks from a multi-parameter perspective. Secondly, a similar analysis was performed for the corresponding systems with production wax, deposited from a crude oil in the North Sea. This allowed to understand the similarities and the differences between the model macrocrystalline wax and the production wax encountered in pipeline operations. A comparison between crystal networks precipitated by evaporation and crystal networks precipitated using the cold finger method was also performed to compare conditions for wax deposition.

2. Experimental section

2.1. Materials

The solvent used in this study was toluene (anhydrous, 99.8%) from Sigma Aldrich, the Netherlands. Macrocrystalline wax was provided by Sasolwax from Sasol, Germany (wax 5405). Literature provides further information on the composition and main properties of wax 5405 from Sasol [23]. The production wax used in this study was provided by an industrial partner and represents a deposit collected from a pig lock at a crude oil field on the Norwegian continental shelf. The compositional characterization of the two waxes was determined by analysis at SGS France and is presented in Table 1. One can notice a lower content of hydrogen and a higher content of nitrogen and sulfur for the production wax, which suggested contamination with resins and asphaltenes. The content of resins/asphaltenes can be estimated at about 10–15% if one assumes a mixture of macrocrystalline wax with 14.8% hydrogen (carbon: hydrogen atom ratio = 2:1) and resins/asphaltenes with 7.7% hydrogen (carbon: hydrogen atom ratio = 1:1). Moreover, the iron content in production wax was at least 200 times higher than in model wax, suggesting contamination with iron and iron oxides particles which could interfere with wax crystallization.



Asphaltenes were obtained by precipitation from a crude oil (API 19°) originating from the Norwegian continental shelf of the North Sea, using n-hexane (HPLC grade, ≥97%), and the same procedure as reported before [19]. Properties of the asphaltenes used in this study can be found in literature [24,25]. The pour point depressant was based on polycarboxylate (proprietary) from BASF, Germany and was presented before as PPD A by Ruwoldt et al. [23] and as PPD by Savulescu et al. [19]. The PPD was purified with solvent, using the procedure described in literature [23]. All concentrations presented in this study are in weight percentages (%wt).

The mica substrate for AFM scanning was acquired from Nano-AndMore GmbH, Germany and had a V1-grade quality and a thickness of 0.15–0.21 mm.

2.2. Sample preparation

Samples for atomic force microscopy were prepared using two main methods: evaporation and cold finger. All the samples were prepared at

Table 1
Elemental and aspect analysis for model wax and production wax.

Element	Model wax	Production wax
Carbon	85.3%	85.5%
Hydrogen	14.8%	14.0%
C:H atom	1:2.08	1:1.96
Nitrogen	<0.05%	0.06%
Oxygen	<0.2%	<0.2%
Sulfur	<0.1%	0.15%
Iron	<5 mg/kg	1127 mg/kg
Aspect	White - 	Brown - 

least 2 times. Each of the atomic force microscopy scans were performed at least 2 times at the same point.

2.2.1. Preparation of samples by evaporation

To prepare the samples with the “evaporation” method, asphaltene and PPD were first dissolved in toluene. Stock solutions with a concentration of 1.05% and 2.1% were prepared. The stock solutions were shaken overnight at 200 rpm to ensure complete dissolution. Then, a range of wax-PPD and wax-asphaltene solutions were prepared by dilution of the initial solutions, followed by the addition of macrocrystalline wax and heating at 60 °C for an hour. For systems containing production wax, 80 °C was used instead, due to difficulties to obtain complete dissolution at 60 °C. A range of wax-only solutions were prepared by dissolution of wax in toluene, followed by heating at either 60 °C (model wax) or 80 °C (production wax). The concentration of wax in all prepared solutions was fixed at 5% for model wax and at 2% for production wax. The concentrations of modifier (asphaltenes and PPDs) were fixed so that the ratio between wax and modifier remains constant in systems with model wax and in systems with production wax. Thus, the values are 0.1%, 0.5%, 1% and 2% for asphaltenes with model wax, 0.04%, 0.2%, 0.4% and 0.8% for asphaltenes with production wax. One additional concentration of 1.6% was used for production wax. For PPD, 1% was used with model wax, while 0.4% was used with production wax.

After the solutions were heated, 3 droplets of each solution were added on a mica substrate. The resulting system was stored in a closed box at room temperature for 2 hours to promote evaporation. Then, to promote wax crystallization, the system was placed in a closed box in the fridge at 5 °C overnight (for approximately 18 hours). Before the AFM scan, the system was placed at room temperature for 2 hours, to reach equilibrium. All samples were in solid state from a macroscopic point of view, before scanning with AFM.

2.2.2. Preparation of samples by the cold finger method

The principles of the cold finger method were presented before in literature [26,27].

Stock wax and wax-PPD solutions were prepared, using the method described before. The quantities used for the cold finger exceeded 500 mL per experiment, which made it impractical and unsustainable to use asphaltenes extracted from crude oils for this part of the study: about 8 litres of hexane would have had to be used to extract asphaltenes per individual experiment.

The solutions were placed in a jacketed glass which was heated using a water/diethylene glycol mixture, circulated through the outside wall and heated at 50 °C, using a water bath. A metal cold finger was cooled to 0 °C by a water/diethylene glycol flow connected to a second water bath. Mica was glued to the bottom of the cold finger. The system was allowed one hour to reach thermal equilibrium and the temperatures were checked with a thermometer before the start of the experiment. To collect a wax or wax-PPD sample, the cold finger was inserted for 2 minutes into the wax and wax-PPD solutions heated at 50 °C. The resulting gel deposited on mica was allowed to evaporate for 1 hour at room temperature and then it was stored in the fridge at 5 °C. Before AFM scanning, the sample was left to stabilize at room temperature for 2 hours.

The purpose of using cold finger was the closer mimicking of pipeline conditions. During fluid transport, a temperature gradient often arises between the inner warmer fluid and the colder pipeline wall. This induces wax deposition on the wall of the pipeline [28]. The cold finger simulates this process by continuously stirring the warmer fluid, while inducing a strong temperature gradient only at the cold finger surface. This is a different mechanism than fluid gelation, which occurs in industry during pipeline shutdown, when the fluid is allowed to rest at increasingly lower temperature. The saturation limit of the wax is reached and crystallization starts, resulting in a gel matrix, in which the other dissolved crude oil components are often trapped [28]. Therefore,

the evaporation method mimics gelation to a higher extent, while the cold finger method mimicks deposition to a higher extent.

2.3. Atomic force microscopy

Atomic force microscopy (AFM) provides mechanical imaging by raster-scanning a surface with a sharp tip which is attached to the end of a cantilever. Once the tip engages with the underlying surface, intermolecular forces between the 2 surfaces arise. These forces lead to the bending of the cantilever, which is tracked by a laser and a piezoelectric detector. This method generates very precise visualization of the surface topography, down to the nanometric or even atomic scale [29–32]. Moreover, AFM allows the quantification of various physical properties related to the molecular interactions when the tip is engaged in the surface. The technique detects a force-distance curve which tracks the change in force as a function of the distance the tip travelled towards or inside the surface. An elasticity analysis of the approach force-distance curve can result in the quantification of the Young Modulus of the surface at the desired locations [33–35]. As the tip detaches from the surface, an attractive force arises, typically corresponding to adhesion that opposes tip retraction. AFM allows for quantification of this force from retract force-distance curve data [36,37].

In this study, a Bio AFM NanoWizard 4 XP was used. The chosen mode of operation was Quantitative Imaging Mode (QI™-mode), with which a force-distance curve was recorded for every pixel along the height map. The scan was performed on consecutive pixels on 128 lines, consisting of 128 pixels each. Transition from one line to another was performed by moving to the first pixel above the last recorded pixel on the previous line. The scanning direction was thus switched on every new line. The setpoint force at which the tip stopped engaging was 1000 nN, the height at which the tip was positioned at the start of each approach (z-length) was 1000 nm. The speed of scanning over the surface was 80 $\mu\text{m/s}$ and the size of the scanning surface was 100 $\mu\text{m} \times 100 \mu\text{m}$ for all systems presented in this study.

The scans were obtained using a silicon PPP-NCH-AuD tip from NanoAndMore GmbH, Germany, with a nominal force constant of 42 N/m, which ensured that any molecular interactions of the tip with the crystal network surface do affect the deflection. The approach force-distance curves were recorded at each pixel, detecting the surface of wax, wax-asphaltene, wax-PPD and asphaltene crystals and generating approach and retract force distance curves. Young Modulus of the approach region and adhesion were quantified using JPK-SPM (now Bruker) software. For elasticity analysis, the stiffness (Young Modulus) of the analyzed surface was estimated by fitting the Hertz model [35] to the force-distance curve obtained at a specific point. The Poisson ratio was assumed to be 0.5 [33], while the radius of the tip was assumed to be 7 nm, which was provided as a radius maximum by the tip manufacturer. For model wax and model wax-asphaltene samples, 2 regions were selected on the approach force-distance curve, corresponding to 2 different Young Modulus profiles. The borders of these regions are presented in Table S1 in the Supplementary Material. The borders were selected after adjustments in the baseline and the contact point, using “Baseline Subtract” and “Contact Point Extend” functions in JPK-SPM Data Processing software. The calculation of Young Modulus for the first region of the model wax and model wax-asphaltene systems was performed by batch processing of the 16384 force-distance curves (the full image) for Slope 1. This allowed for higher accuracy of the measurement. The rest of the Young Modulus calculations were performed by selecting 6 randomized force-distance curve indexes in 2 parallels of the same system (force-distance curve nr. 5000, 10000 and 15000 in 2 parallels of the sample) and then by manual calculation. The error was calculated as the deviation between the 2 samples prepared as described in Section 3.1.1.

The data processing and analysis for the height and adhesion were conducted with the JPK-SPM data processing software (JPK instruments, now Bruker) and with Gwyddion 2.62. The latter was used for the

quantification of 2D Fourier Transforms of the height image. The values presented in this study represent the modulus of the 2D Fast Fourier Transform function in Gwyddion 2.62. JPK-SPM data processing software was used for the rest of data processing and analysis. A reference of 100 $\mu\text{m} \times 100 \mu\text{m}$ was used for height map size in all the height images presented in this article.

The 2D Fast Fourier Transform (FFT) function transformed the height image into a 2D FT image, illustrating spatial frequencies on the x- and y- axis and the logarithmic height amplitude on the contour map, as one can notice in Fig. 1, for example. The mathematic principles behind the 2D FFT could be found in literature [38]. For this study, the focus was placed on the quantification of the frequencies of each height amplitude in the image. To achieve this at a more precise scale, a cross section through the 2D FFT was taken diagonally and the distance between 2 repeating spatial domains with the desired amplitude was calculated [39]. For example, in Fig. 2, to determine the frequency of a height of a desired value (i.e. 3.7 μm) on the diagonal, one had to identify the corresponding amplitude on the cross-section and calculate the distance in spatial frequency between 2 identical amplitude values on the two sides of the image center. This distance represents the inverse of the frequency of the desired height amplitude. In Fig. 2, the blue double arrowed line which connected the 2 identical amplitude values on the two sides of the center had a length of 0.14 cycles/ μm in spatial frequency. This implied that 1 cycle corresponding to one amplitude of 1 μm repeated at an average of $1/0.14 = 7.14 \mu\text{m}$ in the diagonal direction. Some uncertainties arise with the quantification of the frequency for high height values ($>1 \mu\text{m}$), mainly due to the low number of points available in the 2D FFT in this height region.

The reason why the diagonal cross-section was used for this study is that the 2D FFT function had an artefact on the horizontal and vertical planes. Fig. 1 showed that a cross with a vertical component and a horizontal component appeared in the 2D FFT. This cross was an edge artefact, generated by the fact that the 2D FFT is calculated after “gluing” the original height image to itself to infinity on the top, bottom, left and right sides [40,41]. This created a false gradient between the left and right edges of the height image and between the top and bottom edges of the image, which resulted in high intensity frequencies artefacts in the horizontal and vertical directions. A potential removal of this artefact would have required removal of critical frequencies [40]. Using the diagonal cross-section minimizes the artefact effects from the horizontal and vertical directions, while keeping the original height image intact. Moreover, when “glued” towards infinity, the corners of an image, which are the ends of the diagonal, only share 1 point with the next “glued” image, reducing the false gradient to the highest possible extent. The diagonal was representative for the entire FFT which was by definition symmetrical around the center, but in this case was also quasi-symmetrical around the horizontal and vertical axis (Fig. 1).

3. Results and discussion

3.1. Development of analysis methodology for systems based on model wax

This section focuses on the analysis for surfaces evaporated from solutions based on model wax and inhibitors (asphaltene and PPD) in toluene. The analysis in this section represents a novel methodology for the characterization of surface features of wax and wax-inhibitor crystal networks and complements previous NMR studies [8,19,42]. Wax systems have been analyzed with AFM before [31], but the analysis of wax-inhibitor systems represents a novelty in the field. The effect of crystal modifier on the surface features of the wax crystal network is particularly emphasized in this section. The focus parameters are height, frequency of the height, Young Modulus and adhesion. This methodology will be used in Section 3.2. for the investigation of a selected production wax sample, whose exact composition is unknown.

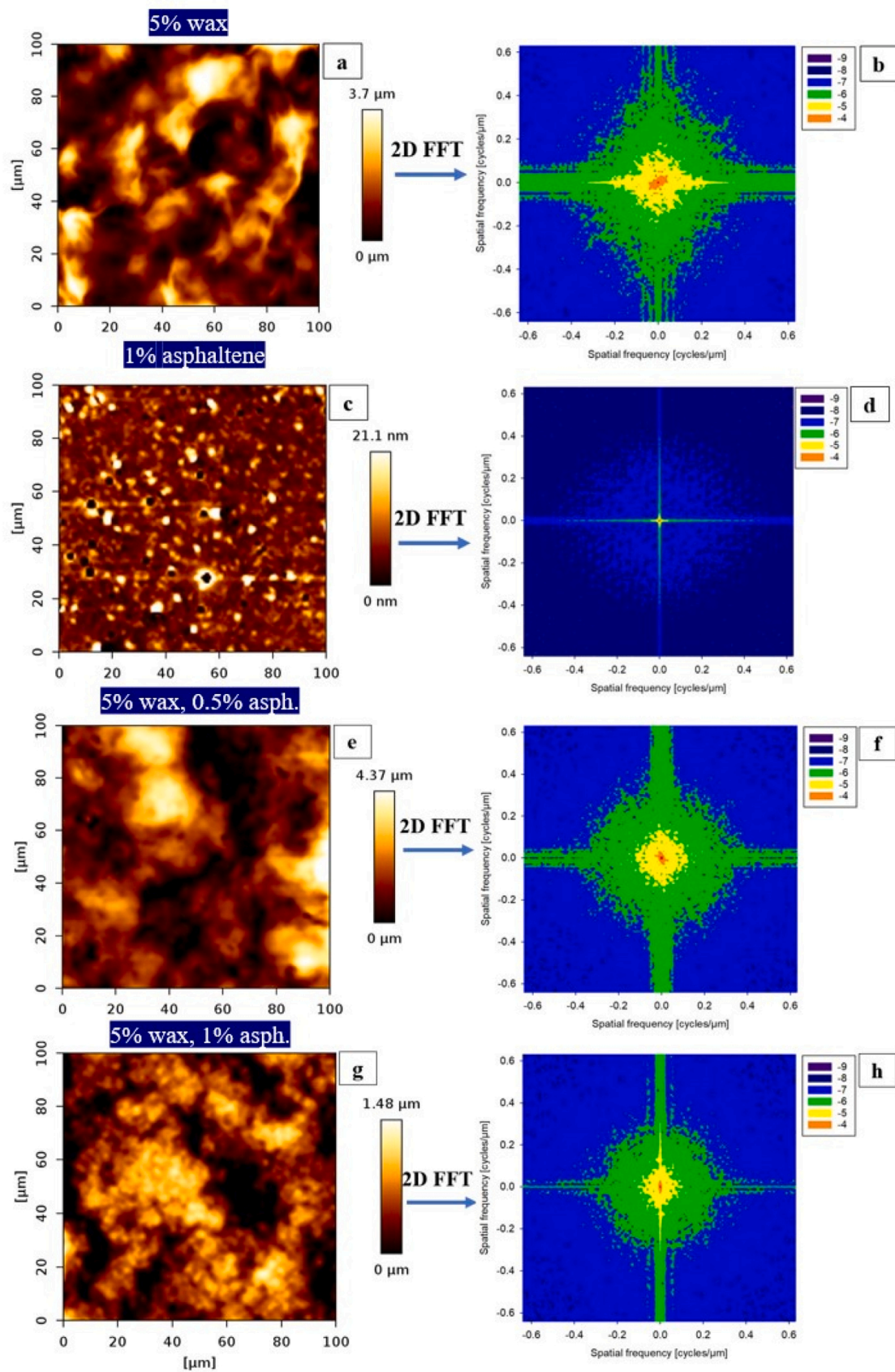


Fig. 1. Height features of the solid surface evaporated from 5% model wax in toluene – (a) height map, (b) 2D Fast Fourier Transform of height map; Height features of the solid surface evaporated from 1% asphaltene in toluene – (c) height map, (d) 2D Fast Fourier Transform of height map; Height features of the solid surface evaporated from 5% model wax, 0.5% asphaltene in toluene – (e) height map, (f) 2D Fast Fourier Transform of height map; Height features of the solid surface evaporated from 5% model wax, 1% asphaltene in toluene – (g) height map, (h) 2D Fast Fourier Transform of height map.

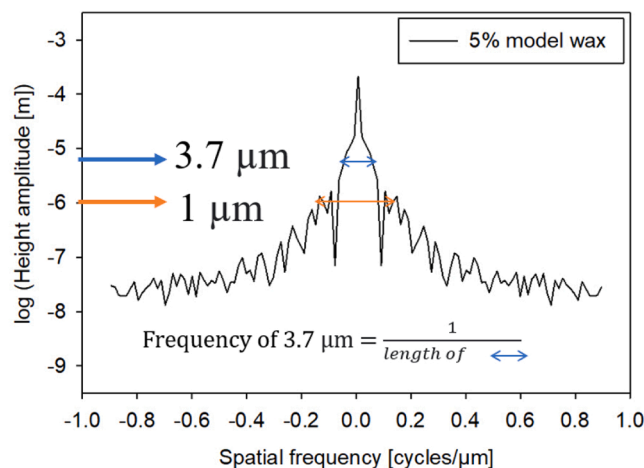


Fig. 2. Diagonal cross-section (from bottom left to top right) of 2D Fast Fourier Transform for the surface evaporated from 5% model wax in toluene.

3.1.1. Characteristics of pure model wax and asphaltenes surfaces

The topographies of wax and asphaltene had significant differences (Fig. 1a,c). For wax, topography indicated needle-like surface features with high aspect ratio and a large maximum height, in the range of μm . This value corresponded to maximum variations on the surface of the wax crystal networks and was likely to have a relationship to crystal height. Wax crystal networks had wide gaps between individual crystals (Fig. 1a,c), induced by limitations in the geometry of the packing. The topography of macrocrystalline wax in Fig. 1a was consistent with previous SEM scans [22,43], which also highlighted the presence of large pores. Recent studies [43] also showed that wax with straight alkane chain had larger pore size and thickness in the crystal network than wax with branched chain. In this study, the macrocrystalline wax composed of mostly straight alkane chain. This explained the large, steep pores and large thickness, which one could notice qualitatively in Fig. 1a. On the other hand, the asphaltene surface (Fig. 1c) had grainy, round features with more uniform distribution and a significantly lower maximum height, in the range of tens of nm. The asphaltene topography and size were comparable to other studies of asphaltenes [44].

The 2D Fourier Transforms in Figs. 1b and 1d were used to estimate the frequencies of the maximum heights on the diagonal, following the algorithm summarized in Fig. 2. Results showed that the frequency of the maximum height in the wax surface was about 3–4 times lower than the frequency of maximum height in the asphaltene surface (Figure S1 a, b in the Supplementary Material). This proved that the height peaks in asphaltenes were more uniform than in wax. Thus, wax formed crystal networks composed of large crystals with large pores between individual crystals [23,43]. On the other hand, asphaltenes were more likely to adsorb on mica, a polar substrate, through their polar moieties, generating a surface with multiple, scattered grains, which did not resemble a crystal network.

Force analysis highlighted a novel distinctive feature for surfaces of wax crystal networks. A 2-slope profile was observed when the tip was approached on the surface (Fig. 3). A lower slope profile emerged at the top of the crystal network surface, while a higher slope profile dominated the remaining distance until the tip fully engaged inside the surface. An explanation for the lower slope was the formation of a softer, amorphous nano-layer (layer 1), on top of the crystals, consisting of wax molecules that did not fully crystallize or of crystals that still trapped a considerable amount of gel or even dissolved wax particles. Previous studies suggested that wax crystal networks could trap dissolved or gel-like phases (crude oil, wax in gel state, dissolved wax, solvent), due to pores induced by crystal packing geometry or due to pores on the crystals [8,43]. Another hypothesis reported that an outer, amorphous layer on the crystal strengthens the gel structure that contributes to

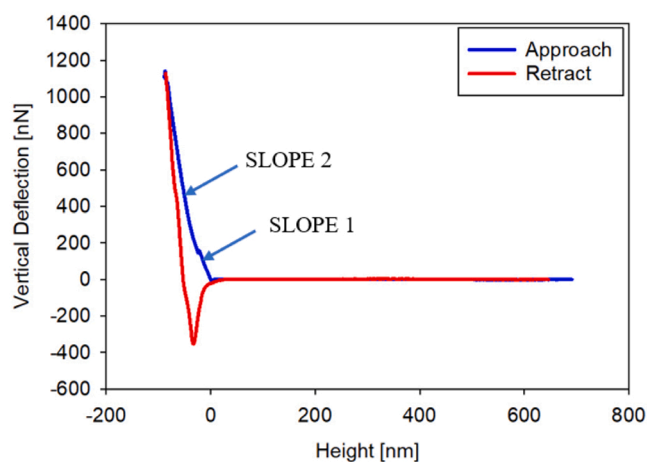


Fig. 3. Force-distance profile for the surface evaporated from 5% model wax in toluene (random selection of a single force-distance curve for the illustration of typical 2-slope profile).

trapping [8]. The analysis of the Young Modulus with AFM could explain all of the above hypotheses. The bottom layer (layer 2) had a different elasticity profile than the top layer (layer 1). Layer 2 corresponded to high Young Modulus values (Table 2, Fig. 4), which formed a stiff layer. Thus, by assuming a positive relationship between the Young Modulus and the degree of crystallinity [45,46] layer 2 represented more crystalline phases of wax. The Young Modulus for layer 2 in wax was still 10–30% lower than for the single layer of wax-PPD (Table 2). One of the potential causes could be the presence of some amorphous phases in wax even in the second layer. Previous NMR studies solidified this hypothesis, by showing that solid macrocrystalline wax had a content of 15–20% of amorphous phase at room temperature [42]. For layer 1, the Young Modulus almost halved in value, relative to layer 2, suggesting the presence of more amorphous phases, which did not fully crystallize. This was most likely due to trapping of dissolved/gel wax. Layer 1 was a nano-scale layer with a thickness representing about 50 nm, which corresponded to less than 2% of the crystal size (Fig. 5, Fig. 1a). As NMR studies showed, amorphous phases were present in a significant percentage (15–20%) in the entire sample, affecting the elasticity of the bottom layer as well. The significant decrease in elasticity in the upper layer with relatively very small thickness should therefore be caused by an event with significantly larger influence in this upper region than in the lower region. Trapping of dissolved wax/gel which could not reach full crystalline phase due to steric hindrance from the other wax molecules was the most likely phenomena behind this behavior.

The thickness of the 2 layers recorded on the force-distance curve had comparable values (Fig. 5). However, the second layer most likely extended deeper inside the surface. The reason why the tip stopped engaging at the measured thickness point is that the force setpoint was reached. The asphaltene surface had a 1-slope profile with a higher Young Modulus than both wax layers (Table 2, Fig. 4). This was consistent with the observation of grainy structures adsorbed on the mica surface. A relationship between the Young Modulus and the height has been investigated. However, only a very weak correlation could be

Table 2

Young Modulus and distance of approach curve for model systems with a 1-slope profile: surfaces evaporated from 1% asphaltene in toluene and 5% model wax, 1% PPD in toluene.

System	Young Modulus [GPa]	Distance for approach force [nm]
1% asphaltene	1.36±0.01	41.7±0.1
5% model wax, 1% PPD	1.14±0.08	66.8±6.9

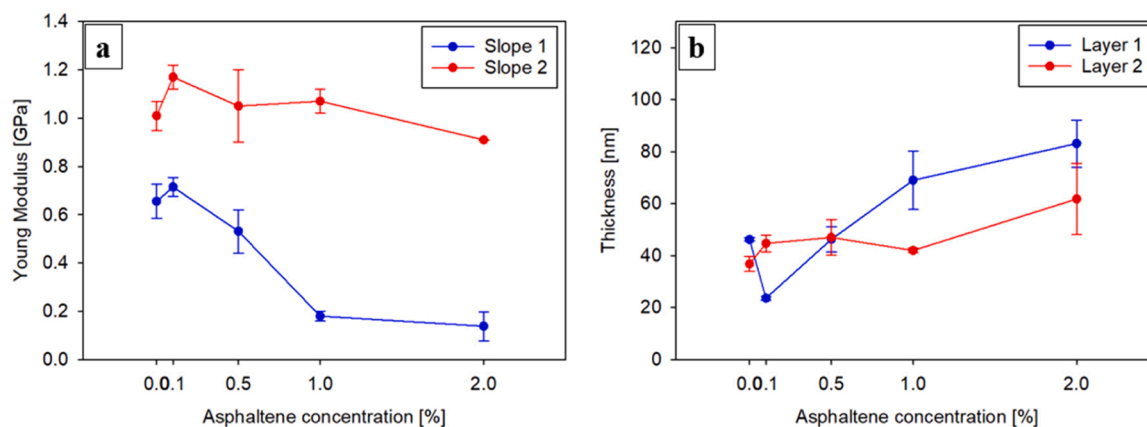


Fig. 4. (a) Average Young Modulus for slope 1 and slope 2 as a function of asphaltene concentration in surfaces evaporated from model wax and model wax-asphaltene solutions in toluene; (b) Average thickness for layer 1 and layer 2 as a function of asphaltene concentration in surfaces evaporated from model wax and model wax-asphaltene solutions in toluene.

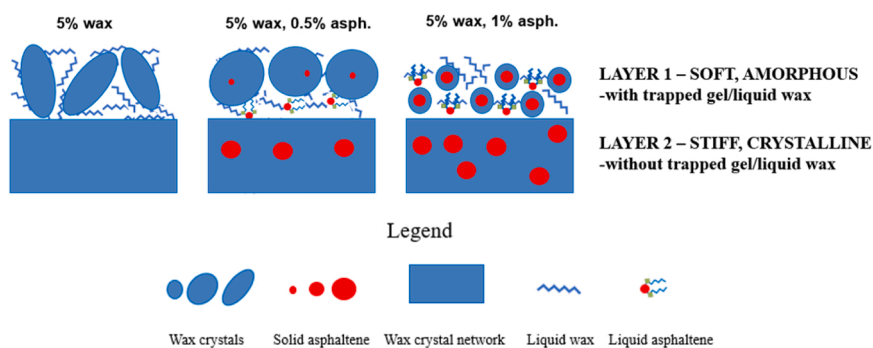


Fig. 5. Schematic representation of the 2-layer profile at the top of surfaces evaporated from model wax and model wax-asphaltene solutions in toluene.

established, highlighting an inconsistent positive trend between the Young Modulus and the height. This proved higher likelihood for amorphous phases with low Young Modulus to accumulate at low height (pore valleys).

The analysis of adhesion data presented in Figure S2 in the Supplementary Material illustrated that the wax surface had significantly higher adhesion than asphaltene. This could be correlated with the presence of amorphous phases, which generated viscous forces [47,48] when the tip was retracted. This was not the case for asphaltenes, which had a stiff surface, without intermediate phases.

3.1.2. Influence of asphaltenes on crystal networks of model wax

The wax-asphaltene surface at 0.5% asphaltene had similarities to wax (Fig. 1a-b, e-f). Firstly, the maximum height was in the same range (4.37 μm , compared to 3.7 μm for wax). Secondly, one could still observe needle-like formations with high heights, although the frequency of individual continuous structures was lower than for wax-only systems, due to crystal network alteration by asphaltenes. To prove this, the 2D Fourier transform indicated a smaller yellow region than for wax-only, corresponding to slightly lower (1.3–1.7 times) average frequency for the maximum height (Figure S1 a, c in the Supplementary Material). This demonstrated more uniformity on the surface. Moreover, the aspect ratio of crystals was lower than in the wax-only surface. Nonetheless, the frequency of intermediate features, depicted by the green area (0.3–3 μm) in Fig. 1b was in the same range as for wax (Fig. 1b). This suggested that intermediate size features were as frequent as for wax, demonstrating a rather low level of deviation from the surface features of wax crystal networks. Pores were as wide or even wider with similar thickness, but with slightly lower frequency. The surface on the 2D height image, with very low values (<0.3 μm), which could be associated with

crystal network pore regions, was similar as for wax. This explained previous findings in NMR studies which concluded that 0.5% asphaltene did not have an effect on the capacity of the wax crystal network to trap dissolved wax during crystallization. Moreover, current findings solidified the hypothesis that the presence of pores and their properties (i.e. size, frequency) have a relationship with the amount of dissolved wax with reduced mobility. Similar total pore surface with quasi-similar individual pores were expected to generate a similar amount of trapped dissolved species, which was consistent with NMR findings [19].

Young Modulus analysis consolidated similarities to wax, highlighting a 2-slope profile with low deviations from wax for both slopes (Fig. 4a). The thickness of each nano-scale layer also had similar values as for wax (Fig. 4b). These observations led to the conclusion that the 2 nano-layers of crystals were altered by asphaltene presence to a low extent at this concentration.

The same did not apply to the wax-asphaltene co-crystal surface at 1% asphaltene. The maximum height decreased by 2.5–3 times from wax-only and from wax-asphaltene at 0.5% asphaltene (Fig. 1). Needle-like formations could not be observed anymore. Instead, individual continuous structures with large areas on the 2D height map were scattered over the surface, most likely representing agglomerations of wax-asphaltene co-crystals. Crystal size was significantly lower and crystal shape was rounder, with lower aspect ratios (Fig. 1). The 2D Fourier Transform showed lower frequency for the maximum height than for wax-only (Figure S1 a,d in Supplementary Material). Also, the cross artefact in 2D Fourier Transform (Figs. 1b, 1h) was much weaker and the blue surface area (height <0.3 μm) in the 2D FT was higher than for wax-only. This demonstrated a higher level of surface uniformity and that heights in the range of 0.1–0.3 μm (upper half of blue region) had the same frequency as higher heights in wax, 0.3–1 μm (lower half of

green region). The pores were thus more frequent in the system with 1% asphaltenes. The likelihood for pores with smaller surface to form was also higher, since the blue region in the 2D FFT was stronger. Additionally, the height of the pores was smaller, as both the height and the FT showed consistently lower height values along the height map. The result was thus the formation of more pores, but with lower volumes. This was consistent with previous NMR findings that showed a strong increase in the amount of trapped wax during crystallization when asphaltene concentration reached 1%. Pores with lower volumes were more likely to induce a decrease in the mobility of dissolved wax.

Young Modulus analysis also deviated from wax significantly, despite following a similar 2-slope profile (Figure S3 in the Supplementary Material). The Young Modulus for the first nano-layer decreased significantly (Fig. 4a), corresponding to a more amorphous upper layer for 1% asphaltene. The thickness of the upper layer also increased by 50% (Fig. 4b), most likely due to a more open, less ordered crystal network structure with more amorphous phases and more trapped dissolved/gel wax, which stimulated additional swelling. The reason for these observations was stronger wax crystal network alteration by asphaltenes in the upper layer, as proposed schematically in Fig. 5. At 1% asphaltene, the asphaltene: wax ratio reached a threshold at which the mechanism of wax-asphaltene co-crystallization changed. Asphaltene nanoaggregates and nanoclusters were present in high quantities from the start of the crystallization process [8]. Thus, a higher amount of wax crystals nucleated on asphaltene nanoaggregates, which were acting as nucleation surfaces. During crystal growth, there was a higher number of non-polar parts of asphaltene molecules to bind wax molecules together, creating altered wax-asphaltene co-crystals, with lower level of wax crystallinity [49]. The earlier formation of large asphaltene clusters and then flocs provided steric hindrance on wax crystals to grow at earlier stages during crystallization. This explained the incapacity of wax crystals to grow towards the upper nano-layer of the surface and the resulting lower crystallinity of wax in this layer. Lower crystal size and rounder shape were also consequences of this mechanism (Fig. 5).

The formation of more amorphous phases on the upper nano-layer could also be linked with the potential presence of dissolved wax which remained trapped in the wax-asphaltene crystal network even after crystallization. NMR findings showed that the quantity of trapped dissolved wax during crystallization was significantly higher at 1% asphaltene than at 0.5% or 0% asphaltene. By combining this fact with the mechanism of crystallization described above, one could conclude that less crystalline phases formed at 1% asphaltene, as a result of high levels of steric hindrance and crystal alteration. The conclusions for model wax and model wax-asphaltene systems at 0.5 and 1% were summarized schematically in Fig. 5.

The trends observed for 1% asphaltenes were either the same or more intense at 2%. Height and 2D Fourier Transform data was presented for the system with 2% asphaltene in Figure S4 in the Supplementary Material. At this concentration, the height decreased even further, by about 30–40%. 2D FT showed higher frequency for the maximum peak than for 1%, with less crystal agglomeration. However, the frequency was similar for identical absolute height amplitudes. Pores with lower volume were more likely to form than for wax-only systems, since the depth was lower and frequencies for low height were higher (blue are in 2D FFT). The FT had weaker cross artefacts, showing an overall more uniform surface. Elasticity analysis showed a similar Young Modulus, but a thicker upper nano-layer than for 1% (Fig. 4). Previous NMR studies [19] indicated an increase in the amount of trapped wax from 1% and 2%. Moreover, the asphaltene content was double at this point. These explained the swelling of the amorphous nano-layer at 2%. The second nano-layer also had a minor decrease in Young Modulus values for the system at 2%. (Fig. 4). This could be caused by either dissolved wax trapping that spread to the bottom layer or by the alteration of individual wax crystals to the point at which they lost elasticity in the entire crystal network.

Adhesion data in Figure S5 in the Supplementary Material indicated that a minor increase in adhesion was observed at 0.1% and 0.5% wax, while a decrease in adhesion occurred at 1% and 2% wax. The decrease at higher concentrations could be explained by the formation of more amorphous phases, with more trapped dissolved wax in the upper nano-layer, which induced weaker viscous forces [47,48] when the AFM tip was retracted.

3.1.3. Influence of PPD on wax crystal network of model wax

The PPD at 1% decreased the maximum height significantly from wax (Fig. 6a,c). The decrease was lower than for asphaltenes at the same concentration (Fig. 1g). However, the 2D Fourier Transform revealed different patterns for PPDs (Fig. 6b,d). Firstly, the cross artefact was hardly noticeable. Secondly, the green region became dominant, but with a smoother transition to the blue region. The first reason for these was higher surface uniformity. The second was the presence of a larger surface with intermediate heights linked to the green region (0.3–3 μ m) than for 5% wax. This corresponded to a more gradual transition between crystal peaks and the pores and inside the crystals. The pores were therefore significantly less steep and wider than for wax or than for asphaltenes. This could be correlated with observations from NMR findings [19] which showed that the wax-PPD co-crystal network did not trap dissolved wax during crystallization. This fact is solidified by the elasticity analysis, which revealed a profile with only 1 slope (Figure S6 in the Supplementary Material), with a Young Modulus, higher than for the stiff layer for wax and wax-asphaltene systems (Table 2). This was an exception from wax and wax-asphaltene systems at all concentrations and could be explained by the lack of large pores which could trap dissolved wax in the upper nano-layer and by the crystallization mechanisms, which deviated from both wax and wax-asphaltene systems. The PPD and the wax form complexes, whose crystal network geometry was more ordered and interlocked in a way which prevented the generation of large confining pores [19,50]. The shape of these complexes was radically different from wax molecules and from bound wax-asphaltene structures, due to the differences between the chemical nature of the PPD and asphaltene. The PPD is a polycarboxylate with long aliphatic chains, while the asphaltene has heteroatoms, aromatic parts and cycloalkanes. Therefore, the PPD had a strong part which interacted with wax (long aliphatic chain) and a strong part which was repulsive to wax (carboxylate). This resulted in more ordered crystal networks, which reached full crystallization. On the other hand, the polydisperse character of asphaltenes prevented an ordered arrangement, generating crystals with more defects. Results from previous NMR studies [19] showed a reduction in the wax crystallization rate generated by PPD addition, which could not be observed with asphaltenes. This was most likely due to high solubility of the PPD through the polar carboxylate groups, which shielded the wax-PPD co-crystals (solvation layer) [6]. Previous NMR studies also showed no trapped wax. The most likely explanation for this is that the more ordered wax-PPD complexes transitioned faster from liquid state to crystalline state, preventing a longer gelation phase in which amorphous layers or pores from the crystals/the crystal network interacted with dissolved wax.

Adhesion analysis revealed lower values for wax-PPD surfaces than for wax-asphaltene surfaces at high asphaltene content (Figures S5, S7 in the Supplementary Material). This could be attributed to lower viscous forces [47] [48]. The wax-PPD co-crystals did not trap dissolved wax, reaching a higher degree of crystallinity than both wax and wax-asphaltene crystal networks.

3.2. Investigation of the applicability of the AFM-based characterization method on production wax samples

Section 3.1.1.–3.1.3 introduced three AFM approaches to characterize properties of model wax, model wax-asphaltene and model wax-PPD surfaces. The focus parameters were height (topography and 2D

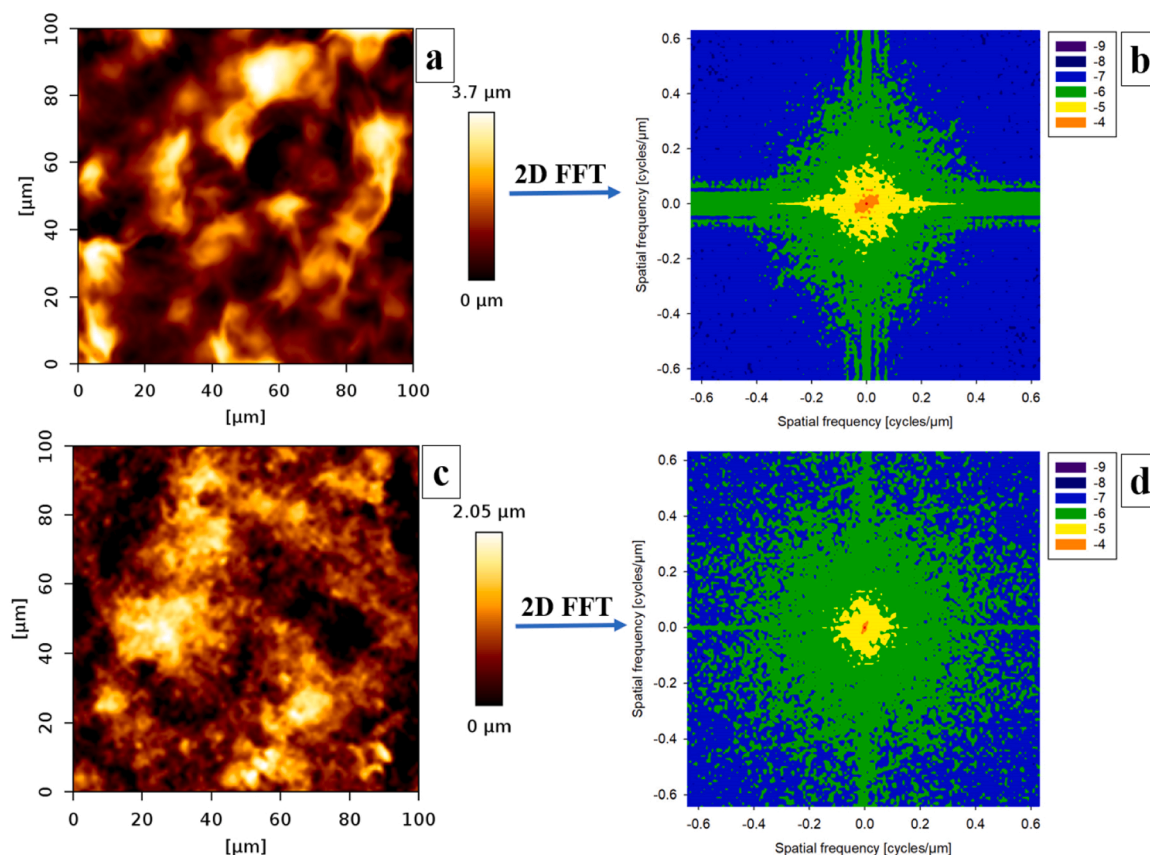


Fig. 6. Height features of the solid surface evaporated from 5% wax – (a) height map, (b) 2D Fast Fourier Transform of height map, 5% model wax, 1% PPD in toluene– (c) height map, (d) 2D Fast Fourier Transform of height map.

Fast Fourier Transform) and Young Modulus on the approach force curve. In this section, all of the above parameters are determined for production wax samples in the presence and in the absence of asphaltenes and PPDs. Surfaces precipitated by cold finger are also analyzed to determine the effects which need to be considered in real pipeline conditions.

3.2.1. Characterization of production wax surfaces generated by evaporation and cold finger

Production wax precipitated by evaporation had comparable crystal size to model wax. However, the topography (Fig. 7a) was different. For model wax, long needle-like structures were formed, while for production wax, the crystal shape was irregular, and crystals were scattered more uniformly over the surface. The frequency of the maximum height was about half, relative to model wax by evaporation (Figure S8a in the Supplementary Material). Higher frequency of intermediate phases could be observed for production wax (stronger region for 0.3–3 μm – green region in 2D FFT in Fig. 7b). The most likely cause for this was the pollution of production wax with 10–15% asphaltenes, resins and iron particles, which altered the crystallization mechanism. Moreover, microcrystalline wax with more branched alkanes could have been present in production wax. This type of wax generates rounder crystals with lower aspect ratios [43,51]. Some effect of asphaltenes could be noticed in Fig. 8a in the way that crystal networks had more scattered surface features, with smaller pores. However, the effects of resins and iron particles was not assessed in this study and should be investigated in the future.

The method for surface generation influenced the height results. Production wax obtained by cold finger precipitation had larger, needle-shaped crystals (Fig. 7c). The cause for this was most likely a change in the chemical composition. The cold finger was in contact with the hot

wax solution only for 2 minutes, which favored the precipitation of high molecular weight wax, with lower solubility. Therefore, low molecular weight waxes, resins, asphaltenes or iron particles were less likely to be present when wax precipitated by cold finger. The result was that crystals were larger than the model macrocrystalline wax crystals and followed a round or a quasi-rectangular shape with an aspect ratio of approximately 2:1, with wide pores. The frequency of the maximum height was about half than for model wax by evaporation (Figure S8b in the Supplementary Material). The crystals were larger and therefore rarer in the scanning size with the same surface. The frequency of intermediate phases in the 0.3–3 μm region was lower in the sample prepared by cold finger (Fig. 7d) than in the sample prepared by evaporation (Fig. 7b), which indicated sharper transitions between crystal peaks and pores in the sample obtained by cold finger. Although the crystal shape for production wax by evaporation deviated significantly from model wax in Fig. 1a, production wax by cold finger resembled it more. This suggested the removal of impurities (resins, asphaltenes, iron) from production wax, when cold finger was used. Further tests remained to be done in the future to confirm this.

Elasticity analysis for production wax revealed a 1-slope profile, but with Young Modulus values that were specific to the upper, amorphous nano-layer of model wax (Table 3). The thickness of the recorded layer was 2–4 times higher than for the upper layer of model wax and 1.5–2 times higher than for the upper layer of model wax with 2% asphaltene, which was the most swollen upper layer identified in model wax-based systems (Table 3, Fig. 5). A multi-layer profile was possible for production wax as well. However, in this case, the AFM reached the maximum force setpoint within the thickness of the first nano-layer. The force setpoint was on the higher range allowed for the AFM instrument and therefore, further studies need to be carried out to identify a potential second layer underneath the upper layer. Nonetheless, the values

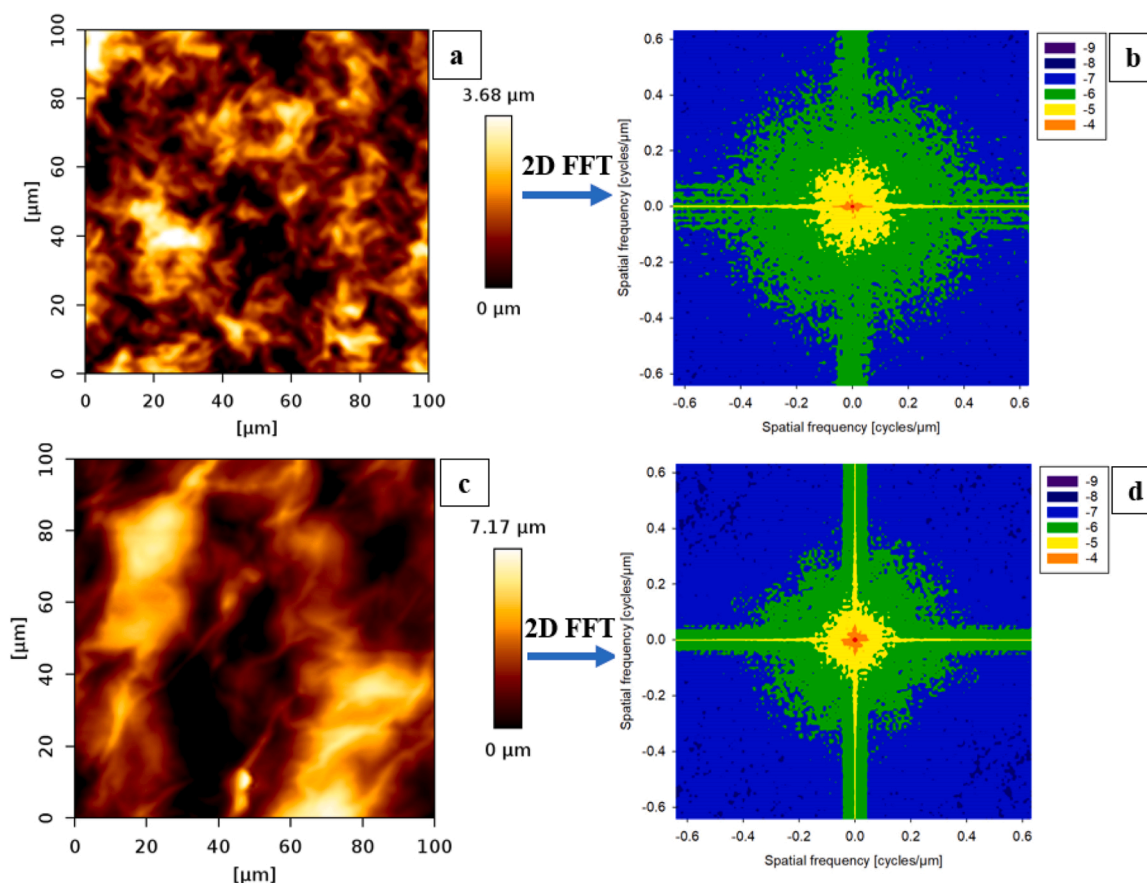


Fig. 7. (a), (b) Height features of the solid surface **evaporated** from 2% production wax in toluene – (a) height map, (b) 2D Fast Fourier Transform of height map; (c), (d) Height features of the solid surface prepared by **cold finger** from 2% production wax in toluene – (c) height map, (d) 2D Fast Fourier Transform of height map.

determined in this study still indicated that a much larger amorphous nano-layer formed for production wax. 2 hypotheses were proposed to explain this. The first was a higher percentage of amorphous phase in the entire sample. This was consistent with the presence of microcrystalline wax in the production sample. Previous NMR studies [42] demonstrated that microcrystalline waxes had a higher amorphous content (30–40%) at room temperature than macrocrystalline waxes (15–20%). The second hypothesis was a higher amount of dissolved wax or gel that was trapped in the crystal network. The potential presence of 10–15% asphaltene in the production wax samples consolidated this theory. More amorphous structures were obtained for the surface prepared by cold finger. This could be explained by the fact that higher molecular weight waxes, precipitated by cold finger, were more likely more micro-crystalline [52]. Additionally, literature reported higher overall Young Modulus by large deformation mechanical testing for straight alkane waxes than for branched alkane waxes, consolidating the conclusions [43]. The values presented in the corresponding study were 2.76 GPa for macrocrystalline wax and 1.64 GPa for microcrystalline wax. This is in the same range as results presented in this study and deviations are most likely caused by differences in chemical composition, preparation method and tip-related assumptions (tip radius, Poisson ratio) used in this study.

3.2.2. Characterization of production wax-asphaltene surfaces generated by evaporation

Production wax crystal networks were less sensitive to asphaltene addition than model wax crystal networks. The addition of 0.8% asphaltene to 2% production wax corresponded to the addition of 2% asphaltene to 5% model wax, in terms of asphaltene:wax weight ratio. However, while the effect on model wax was strong at this

concentration, there was little to no effect on production wax. The crystal size, the height frequency and the crystal shape remained approximately identical (Fig. 7a,b and 8 a,b). More hypotheses could be proposed to explain this phenomenon. Firstly, production wax was likely to contain 10–15% asphaltenes, which could alter the wax crystal network on their own, reducing the impact of the additional asphaltenes. Secondly, resins, iron particles and microcrystalline wax induced a different crystallization mechanism in presence of asphaltenes. Lastly, the absolute asphaltene concentration might play a role in the wax crystallization mechanism. Asphaltenes at 2% formed larger nano-aggregates and nanoclusters than asphaltenes at 0.8%. Thus, production wax might start crystallizing before the asphaltene reached the same nanoaggregate/nanocluster size as it reached when model wax starts crystallizing.

To verify the last hypothesis, an additional asphaltene concentration, 1.6%, was used. The topography at this concentration (Fig. 8c) suggested a minor decrease in crystal size. 2D FFT showed lower frequency for the heights in the 0.3–3 μm region (Fig. 8d - green region in 2D FFT). This demonstrated larger and more shallow crystal network pores, which resembled model wax-asphaltene crystal network at high concentrations. It can thus be concluded that a higher absolute concentration of asphaltenes induced stronger, but still relatively weak crystal network alteration. The 1% concentration point was also indicated before as a threshold for complete asphaltene nanoaggregate/nanocluster formation, which promoted the alteration of the wax crystallization mechanism [8,19].

Elasticity analysis showed the formation of a single layer with Young modulus values which were higher than production wax, but lower than asphaltenes. The thickness of the layer was relatively low in comparison to the other systems based on model and production wax. However, the

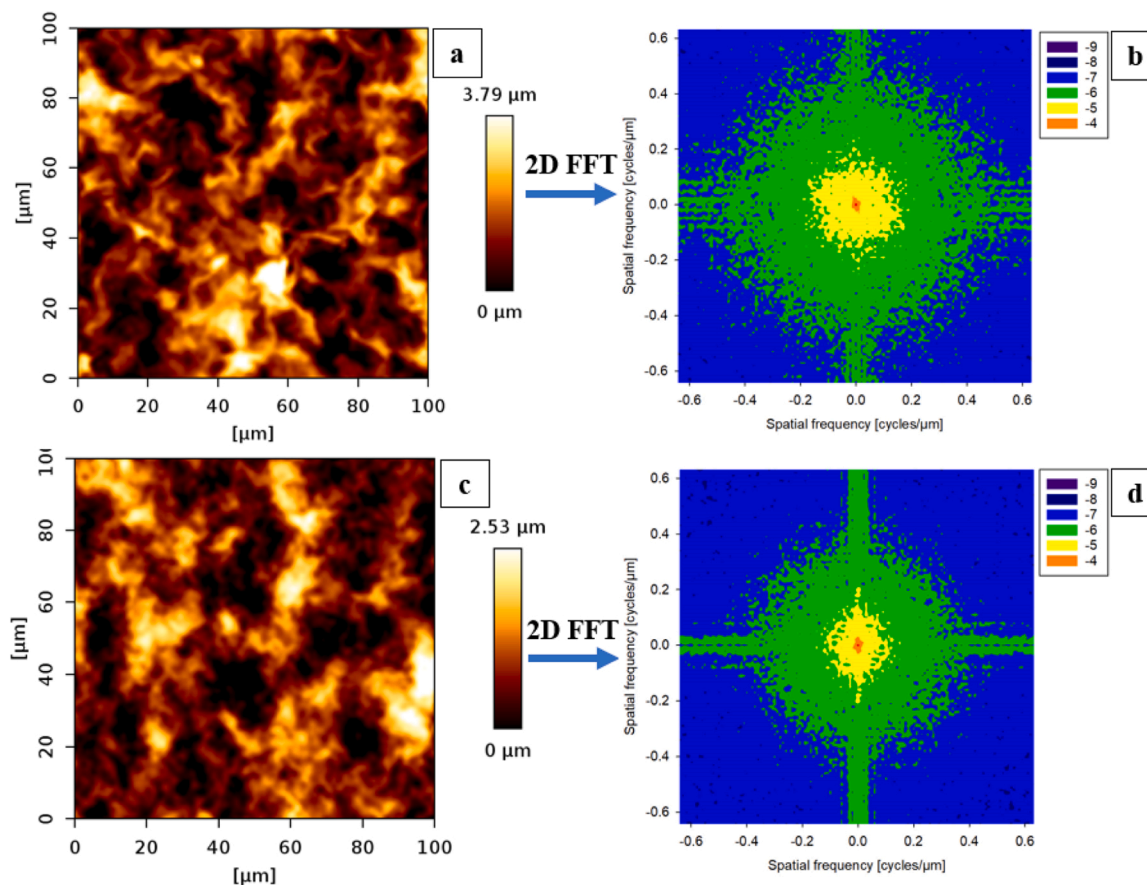


Fig. 8. (a), (b) Height features of the solid surface evaporated from 2% production wax, 0.8% asphaltene in toluene– (a) height map, (b) 2D Fast Fourier Transform of height map; (c), (d) Height features of the solid surface evaporated from 2% production wax, 1.6% asphaltene in toluene - (c) height map, (d) 2D Fast Fourier Transform of height map.

Table 3

Young Modulus and distance of approach curve for systems based on production wax.

System	Young Modulus [GPa]	Distance for approach force [nm]
2% ind. wax - evaporaton	0.71±0.06	105.7±12.1
2% ind. wax – cold finger	0.55±0.01	146.8±50.5
2% ind. wax, 0.8% asph. - evaporation	1.08±0.05	56.0±5.8
2% ind. wax, 1.6% asph. - evaporation	1.17±0.16	46.7±1.2
2% ind. wax, 0.4% PPD - evaporation	0.83±0.07	79.0±7.7
2% ind. wax, 0.4% PPD – cold finger	0.63±0.04	124.8±10.8

value was in the same range as for asphaltenes-alone (Tables 2,3), which suggested that the force setpoint was achieved at the same distance as for asphaltenes. The most likely reason for this was the potential formation of independent asphaltene deposits in the upper layers of production wax. High Young Modulus values (Table 3) suggested that a mixture of independent production wax crystals and asphaltene deposits was most likely present in these nano-layers. This indicated that asphaltenes' influence on wax crystallization reached a maximum at a concentration below 1.6%. The stiff layer also suggested that dissolved wax trapping or the formation of amorphous phases was unlikely for production wax-asphaltene systems.

3.2.3. Characterization of production wax-PPD surfaces generated by evaporation and cold finger

Figs. 9a and 9c showed that the PPD induced a strong decrease in wax crystal size for both sample preparation methods (evaporation and cold finger). The ratio between the maximum crystal size obtained with cold finger and with evaporation remained similar to the model wax-only systems. With evaporation, crystal shape became rounder, more dendritic and thinner than for wax-only. With cold finger, the same tendency could be noticed, but the crystals had higher aspect ratios than with evaporation. 2D FFT analysis showed the cross artefact disappeared almost completely for wax-PPD crystals with evaporation (Fig. 9b), suggesting high surface uniformity. For the sample by cold finger, uniformity was lower. To support this, the 2D FFT also showed a much higher frequency of the maximum height and of intermediate heights (green region: 0.3–3 μm) for the sample by evaporation than for the sample by cold finger (Figure S8 c,d in the Supplementary Material, Fig. 9b,d). The crystal size in the surfaces with PPD was 2–2.5 times lower than in the corresponding surfaces without PPD, regardless of the preparation method. The conclusion was that the PPD induced a similar effect on all types of wax, which was dependent on the crystal size and shape in the initial, untreated wax structure.

The elasticity analysis revealed a 1-slope profile, with Young Modulus values which were 20–30% higher than for production wax alone, but 30–40% lower than for model wax with PPD (Table 2, Table 3). The PPD reduced the preponderance of amorphous phases and led to more crystalline production wax-PPD networks. However, the wax-PPD networks were more amorphous when production wax was used.

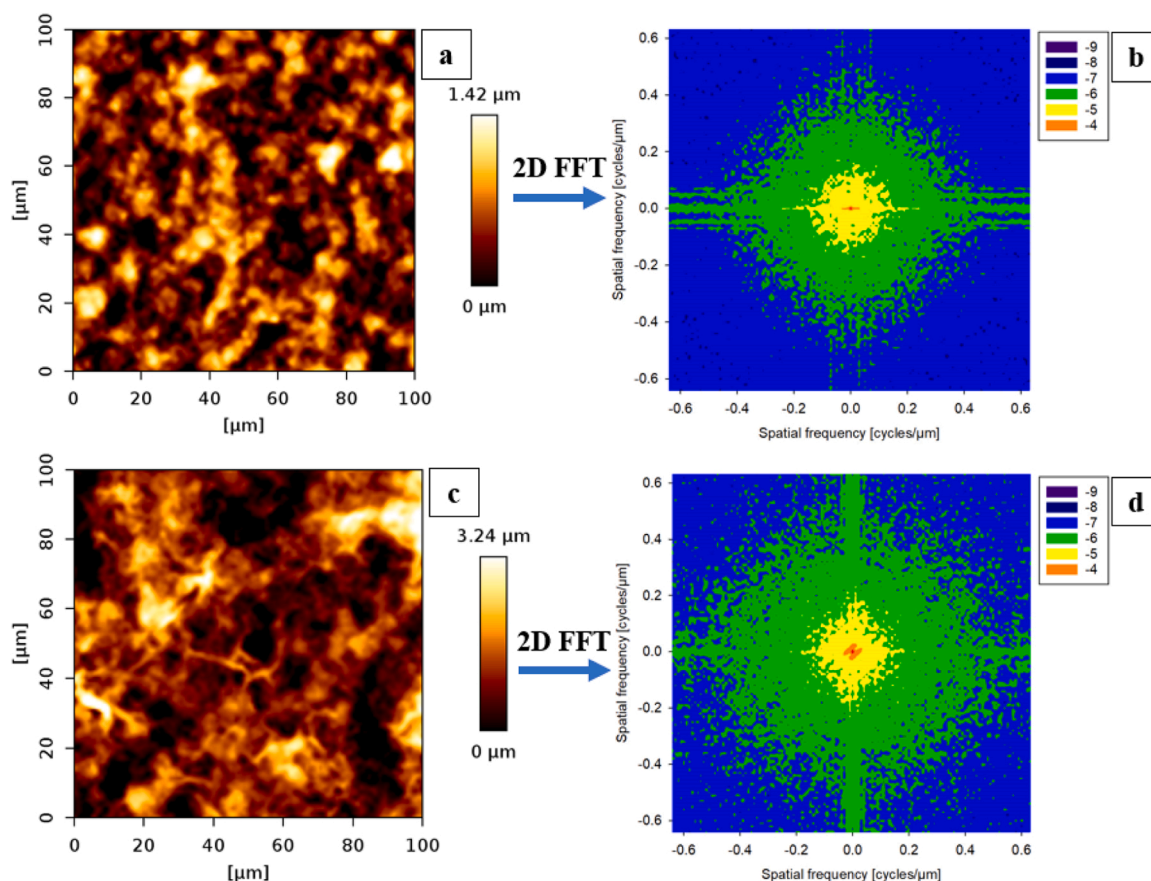


Fig. 9. (a), (b) Height features of the solid surface **evaporated** from 2% production wax, 0.4% PPD in toluene – (a) height map, (b) 2D Fast Fourier Transform of height map; (c), (d) Height features of the solid surface prepared by **cold finger** from 2% production wax, 0.4% PPD in toluene – (c) height map, (d) 2D Fast Fourier Transform of height map.

4. Conclusion

AFM was demonstrated as a reliable quantitative tool for the analysis of surface features of model wax and model wax-inhibitor surfaces. The differences between surfaces were assessed with a focus on topography, elasticity and adhesion and the conclusions were as follows:

- Model wax had large crystals with a needle shape and large aspect ratio. The frequency of crystal peaks was high and the pores in the crystal network were wide and deep, which facilitated the trapping of dissolved wax during crystallization. A 2-layer profile was identified at the crystal network surface. A stiffer, more crystalline nano-scale layer was formed on the bottom, while a softer, more amorphous nano-scale layer was formed on the top, corresponding to wax which did not crystallize completely. A first reason for this was steric hindrance imposed by the already formed wax crystals, which prevented remaining dissolved/gel wax to crystallize completely. A second reason was the establishment of an equilibrium at which dissolved/gel wax remained trapped in the upper layer due to interlocking.
- The addition of a low content of asphaltenes did not modify the crystal size. However, the shape was rounder, and the frequency of crystal peaks was lower. A similar pore area explained the similar amount of trapped wax observed during crystallization [19]. An amorphous layer with similar elasticity was formed, demonstrating a similar wax crystallization mechanism. On the other hand, the addition of a high content of asphaltenes reduced crystal size and modified the shape from needle to round, dendritic. More, narrower, and thinner pores were formed, which explained the increase in the

amount of dissolved wax that this crystal network could trap. A more amorphous upper layer with decreased crystallinity was formed, suggesting an equilibrium in which wax crystal growth was prevented more strongly.

- The addition of PPD resulted in lower crystal size and round, dendritic shape. A more uniform surface with wider, less steep pores was formed. The modified wax-PPD crystal network reached a full crystalline equilibrium, with a stiff and most likely more ordered crystal network, whose development was not disrupted by steric hindrance on gel structures or by dissolved wax trapping.

After the development of the AFM methodology on model systems, applicability for the selected production sample and for wax industrial precipitation conditions (cold finger) was demonstrated. The AFM results showed a high likelihood for high microcrystalline wax content and potential contamination with resins, asphaltenes and iron particles which affected crystal shape (rounder) and frequency (more scattering over the surface). Industrial precipitation conditions led to an initial precipitation of high molecular weight wax, which had very large, rectangular crystals. The effect of asphaltene was weak in this case, most likely due to changes in wax composition. On the other hand, the PPD still had a very strong effect, causing significant crystal size reduction and shape change towards rounder crystals with more uniform crystal network surfaces. Production wax had a larger amorphous layer on top, caused by the presence of microcrystalline phases. Industrial precipitation conditions resulted in an even thicker and more amorphous layer, corresponding to high molecular weight microcrystalline wax. The addition of PPD increased the crystallinity of the nano-layer of production wax, but it was still more amorphous than in model wax systems

with similar PPD content.

The methodology developed in this study could be used and adapted in the future to analyze a range of model and production wax samples. The proposed AFM method creates novelty by introducing a tool to relatively estimate crystal network parameters described in this paper (crystal size, pore size, frequency of size features, elasticity, adhesion). A direct relationship between wax crystal network parameters and rheological properties of waxy fluids is the next step to be taken to establish the effect on macro-scale flow assurance phenomena.

CRedit authorship contribution statement

Sébastien Simon: Writing – review & editing, Visualization, Supervision, Investigation, Funding acquisition, Conceptualization. **Maja Rücker:** Writing – review & editing, Visualization, Supervision, Resources, Investigation, Conceptualization. **George Claudiu Savulescu:** Writing – review & editing, Writing – original draft, Visualization, Validation, Software, Methodology, Investigation, Formal analysis, Data curation, Conceptualization. **Gisle Øye:** Writing – review & editing, Supervision, Resources, Investigation, Funding acquisition, Conceptualization.

Declaration of Competing Interest

The authors declare that they have no known competing financial interests or personal relationships that could have appeared to influence the work reported in this paper.

Data availability

Data will be made available on request.

Acknowledgement

This work is part of SUBPRO SFI, a research-based center within subsea production and processing. The authors hereby acknowledge the financial support from SUBPRO, which is financed by the Research Council of Norway, funding code 237893, major industry partners and NTNU. The authors would also like to acknowledge the multi-scale lab in the Energy Technology group at Eindhoven University of Technology for their support with experimental atomic force microscopy facilities. Moreover, we collaborated with Einar Eng Johnsen (Equinor) who provided the production wax samples.

Appendix A. Supporting information

Supplementary data associated with this article can be found in the online version at [doi:10.1016/j.colsurfa.2024.133843](https://doi.org/10.1016/j.colsurfa.2024.133843).

References

- [1] L. Oliveira, R. Nunes, I. Melo, Y. Ribeiro, L. Guimaraes, J. Dias, R. Guimaraes, E. Lucas, Evaluation of the correlation between wax type and structure/behavior of the pour point depressant, *Fuel Process. Technol.* **149** (2016) 268–274, <https://doi.org/10.1016/j.fuproc.2016.04.024>.
- [2] Kelland, M. *Production Chemicals for the Oil and Gas Industry*; 2009; Vol. 1. <https://doi.org/10.1201/9781420092974>.
- [3] Al-Yaari, M. Paraffin Wax Deposition: Mitigation and Removal Techniques. *Society of Petroleum Engineers - Saudi Arabia Section Young Professionals Technical Symposium 2011* 2011. <https://doi.org/10.2118/155412-MS>.
- [4] K.G. Paso, K.K. Krückert, H.-J. Oschmann, H. Ali, J. Sjöblom, PPD architecture development via polymer–crystal interaction assessment, *J. Pet. Sci. Eng.* **115** (2014) 38–49, <https://doi.org/10.1016/j.petrol.2014.02.002>.
- [5] B. Wei, Recent advances on mitigating wax problem using polymeric wax crystal modifier, *J. Pet. Explor. Prod. Technol.* **5** (4) (2015) 391–401, <https://doi.org/10.1007/s13202-014-0146-6>.
- [6] N. Li, G. Mao, X. Shi, S. Tian, Y. Liu, Advances in the research of polymeric pour point depressant for waxy crude oil, *J. Dispers. Sci. Technol.* **39** (8) (2018) 1165–1171, <https://doi.org/10.1080/01932691.2017.1385484>.
- [7] C. Wu, J. Zhang, W. Li, N. Wu, Molecular dynamics simulation guiding the improvement of EVA-type pour point depressant, *Fuel* **84** (16) (2005) 2039–2047, <https://doi.org/10.1016/j.fuel.2004.12.009>.
- [8] G.C. Savulescu, S. Simon, G. Sørland, G. Øye, Understanding the effect of asphaltenes and wax inhibitors on wax crystallization by improved NMR techniques, *Ind. Eng. Chem. Res.* (2023), <https://doi.org/10.1021/acs.iecr.3c02218>.
- [9] J. Ruwoldt, S. Subramanian, S. Simon, H. Oschmann, J. Sjöblom, Asphaltene fractionation based on adsorption onto calcium carbonate: Part 3. Effect of asphaltenes on wax crystallization, *Colloids Surf. A Physicochem Eng. Asp.* **554** (2018) 129–141, <https://doi.org/10.1016/j.colsurfa.2018.06.025>.
- [10] O.C. Mullins, H. Sabbah, J. Eyssautier, A.E. Pomerantz, L. Barré, A.B. Andrews, Y. Ruiz-Morales, F. Mostowfi, R. McFarlane, L. Goual, R. Lepkowitz, T. Cooper, J. Orbulescu, R.M. Leblanc, J. Edwards, R.N. Zare, Advances in asphaltene science and the Yen–Mullins model, *Energy Fuels* **26** (7) (2012) 3986–4003, <https://doi.org/10.1021/ef300185p>.
- [11] P. Kriz, S.I. Andersen, Effect of asphaltenes on crude oil wax crystallization, *Energy Fuels* **19** (3) (2005) 948–953, <https://doi.org/10.1021/ef049819e>.
- [12] E. Ariza-León, D.R. Molina-Velasco, A. Chaves-Guerrero, Review of studies on asphaltene - wax interaction and the effect thereof on crystallization, *CTyF - Cienc., Tecnol. Y. Futuro. Scieloco* (2014) 39–53, <https://doi.org/10.29047/01225383.32>.
- [13] Y. Lei, S. Han, J. Zhang, Y. Bao, Z. Yao, Y. Xu, Study on the effect of dispersed and aggregated asphaltene on wax crystallization, gelation, and flow behavior of crude oil, *Energy Fuels* **28** (4) (2014) 2314–2321, <https://doi.org/10.1021/ef4022619>.
- [14] H. Cao, X. Cao, X. Zhao, D. Guo, Y. Liu, J. Bian, Molecular dynamics simulation of wax molecules aggregational crystallization behavior during cooling of crude oil mixture, *Case Stud. Therm. Eng.* **37** (2022) 102298, <https://doi.org/10.1016/j.csite.2022.102298>.
- [15] R. Venkatesan, J.-A. Östlund, H. Chawla, P. Wattana, M. Nydén, H.S. Fogler, The effect of asphaltenes on the gelation of waxy oils, *Energy Fuels* **17** (6) (2003) 1630–1640, <https://doi.org/10.1021/ef034013k>.
- [16] G.E. Oliveira, C.R.E. Mansur, E.F. Lucas, G. González, W.F. de Souza, The effect of asphaltenes, naphthenic acids, and polymeric inhibitors on the pour point of paraffins solutions, *J. Dispers. Sci. Technol.* **28** (3) (2007) 349–356, <https://doi.org/10.1080/01932690601107526>.
- [17] M. del C. García, Crude oil wax crystallization. The effect of heavy n-paraffins and flocculated asphaltenes, *Energy Fuels* **14** (5) (2000) 1043–1048, <https://doi.org/10.1021/ef0000330>.
- [18] V. Molina, D. Ariza León, E. Chaves-Guerrero, A. Understanding the effect of chemical structure of asphaltenes on wax crystallization of crude oils from colorado oil field, *Energy Fuels* **31** (9) (2017) 8997–9005, <https://doi.org/10.1021/acs.energyfuels.7b01149>.
- [19] G.C. Savulescu, S. Simon, G. Sørland, G. Øye, New nuclear magnetic resonance approaches on the evolution of wax mobility during wax crystallization, *Energy Fuels* **36** (1) (2022) 350–360, <https://doi.org/10.1021/acs.energyfuels.1c03613>.
- [20] G.C. Savulescu, S. Simon, G. Sørland, G. Øye, Understanding the effect of asphaltenes and wax inhibitors on wax crystallization by improved NMR techniques, *Ind. Eng. Chem. Res.* (2023), <https://doi.org/10.1021/acs.iecr.3c02218>.
- [21] G.C. Savulescu, S. Simon, G. Sørland, G. Øye, New nuclear magnetic resonance approaches on the evolution of wax mobility during wax crystallization, *Energy Fuels* **36** (1) (2022) 350–360, <https://doi.org/10.1021/acs.energyfuels.1c03613>.
- [22] H.R. Jafari Ansaroudi, M. Vafaie-Sefti, Sh Masoudi, T.J. Behbahani, H. Jafari, Study of the morphology of wax crystals in the presence of ethylene-co-vinyl acetate copolymer, *Pet. Sci. Technol.* **31** (6) (2013) 643–651, <https://doi.org/10.1080/10916466.2011.632800>.
- [23] J. Ruwoldt, G. Humborstad Sørland, S. Simon, H.-J. Oschmann, J. Sjöblom, Inhibitor-wax interactions and PPD effect on wax crystallization: new approaches for GC/MS and NMR, and comparison with DSC, CPM, and rheometry, *J. Pet. Sci. Eng.* **177** (2019) 53–68, <https://doi.org/10.1016/j.petrol.2019.02.046>.
- [24] S. Subramanian, G.H. Sørland, S. Simon, Z. Xu, J. Sjöblom, Asphaltene fractionation based on adsorption onto calcium carbonate: Part 2. Self-association and aggregation properties, *Colloids Surf. A Physicochem Eng. Asp.* **514** (2017) 79–90, <https://doi.org/10.1016/j.colsurfa.2016.11.035>.
- [25] F.E. Pinto, E.V. Barros, L.V. Tose, L.M. Souza, L.A. Terra, R.J. Poppi, B.G. Vaz, G. Vasconcelos, S. Subramanian, S. Simon, J. Sjöblom, W. Romão, Fractionation of Asphaltenes in N-Hexane and on Adsorption onto CaCO₃ and Characterization by ESI(+)-FT-ICR MS: Part I, *Fuel* **210** (2017) 790–802, <https://doi.org/10.1016/j.fuel.2017.09.028>.
- [26] J. da S.T. dos Santos, A.C. Fernandes, M. Giuliatti, Study of the paraffin deposit formation using the cold finger methodology for brazilian crude oils, *J. Pet. Sci. Eng.* **45** (1) (2004) 47–60, <https://doi.org/10.1016/j.petrol.2004.05.003>.
- [27] Fan, K.; Huang, Q.; Li, S.; Zhao, D. Wax Deposition Study in a Cold-Finger System with Model Oil. *SPE/IATMI Asia Pacific Oil & Gas Conference and Exhibition*file:///C:/Users/georgecs/Downloads/RevModPhys.75.949.bibtex. October 20, 2015, p SPE-176447-MS. <https://doi.org/10.2118/176447-MS>.
- [28] Kelland, M. *Production Chemicals for the Oil and Gas Industry*; 2009; Vol. 1. <https://doi.org/10.1201/9781420092974>.
- [29] F.J. Giessibl, Advances in Atomic Force Microscopy, *Rev. Mod. Phys.* **75** (3) (2003) 949–983, <https://doi.org/10.1103/RevModPhys.75.949>.
- [30] B. Schuler, G. Meyer, D. Peña, O.C. Mullins, L. Gross, Unraveling the molecular structures of asphaltenes by atomic force microscopy, *J. Am. Chem. Soc.* **137** (31) (2015) 9870–9876, <https://doi.org/10.1021/jacs.5b04056>.
- [31] M. Žbik, R.G. Horn, N. Shaw, AFM study of paraffin wax surfaces, *Colloids Surf. A Physicochem Eng. Asp.* **287** (1) (2006) 139–146, <https://doi.org/10.1016/j.colsurfa.2006.03.043>.

- [32] G.C. Savulescu, M. Rücker, A. Scanziani, R. Pini, A. Georgiadis, P.F. Luckham, Atomic force microscopy for the characterisation of pinning effects of seawater micro-droplets in n-decane on a calcite surface, *J. Colloid Interface Sci.* 592 (2021) 397–404, <https://doi.org/10.1016/j.jcis.2021.02.070>.
- [33] E.M. Ekanem, M. Rücker, S. Yesufu-Rufai, C. Spurin, N. Ooi, A. Georgiadis, S. Berg, P.F. Luckham, Novel adsorption mechanisms identified for polymer retention in carbonate rocks, *J. Colloid Interface Sci.* 4 (2021) 100026, <https://doi.org/10.1016/j.jcis.2021.100026>.
- [34] S. Yesufu-Rufai, F. Marcellis, A. Georgiadis, S. Berg, M. Rücker, J. van Wunnik, P. Luckham, Atomic force microscopy (AFM) study of redox conditions in sandstones: impact on wettability modification and mineral morphology, *Colloids Surf. A Physicochem Eng. Asp.* 597 (2020) 124765, <https://doi.org/10.1016/j.colsurfa.2020.124765>.
- [35] Y.M. Efremov, W.-H. Wang, S.D. Hardy, R.L. Geahlen, A. Raman, Measuring nanoscale viscoelastic parameters of cells directly from AFM force-displacement curves, *Sci. Rep.* 7 (1) (2017) 1541, <https://doi.org/10.1038/s41598-017-01784-3>.
- [36] B. Cappella, G. Dietler, Force-distance curves by atomic force microscopy, *Surf. Sci. Rep.* 34 (1) (1999) 1–104, [https://doi.org/10.1016/S0167-5729\(99\)00003-5](https://doi.org/10.1016/S0167-5729(99)00003-5).
- [37] P.A. Maurice, Applications of atomic-force microscopy in environmental colloid and surface chemistry, *Colloids Surf. A Physicochem Eng. Asp.* 107 (1996) 57–75, [https://doi.org/10.1016/0927-7757\(95\)03372-6](https://doi.org/10.1016/0927-7757(95)03372-6).
- [38] Rao, K.R.; Kim, D.; Hwang, J.-J. *Fast Fourier Transform - Algorithms and Applications*; 2010. <https://doi.org/10.1007/978-1-4020-6629-0>.
- [39] P. Kaspar, D. Sobola, P. Sedlák, V. Holcman, L. Grmela, Analysis of color shift on butterfly wings by Fourier transform of images from atomic force microscopy, *Microsc. Res. Tech.* 82 (12) (2019) 2007–2013, <https://doi.org/10.1002/jemt.23370>.
- [40] Mahmood, F.; Toots, M.; Öfverstedt, L.-G.; Skoglund, U. 2D Discrete Fourier Transform with Simultaneous Edge Artifact Removal for Real-Time Applications. In *2015 International Conference on Field Programmable Technology (FPT)*; 2015; pp 236–239. <https://doi.org/10.1109/FPT.2015.7393157>.
- [41] J.K. Pijanka, P.P. Markov, D. Midgett, N.G. Paterson, N. White, E.J. Blain, T. D. Nguyen, H.A. Quigley, C. Boote, Quantification of collagen fiber structure using second harmonic generation imaging and two-dimensional discrete fourier transform analysis: application to the human optic nerve head, *J. Biophotonics* 12 (5) (2019) e201800376, <https://doi.org/10.1002/jbio.201800376>.
- [42] G.C. Savulescu, S. Simon, G. Sørland, G. Øye, Novel nuclear magnetic resonance techniques to assess the wax precipitation evolution in crude oil systems, *Energy Fuels* 37 (1) (2023) 291–300, <https://doi.org/10.1021/acs.energyfuels.2c03309>.
- [43] Y. Miyazaki, A.G. Marangoni, Structural-mechanical model of wax crystal networks—a mesoscale cellular solid approach, *Mater. Res Express* 1 (2) (2014) 25101, <https://doi.org/10.1088/2053-1591/1/2/025101>.
- [44] M.-H. Ese, J. Sjöblom, J. Djuve, R. Pugh, An atomic force microscopy study of asphaltene on mica surfaces. Influence of added resins and demulsifiers, *Colloid Polym. Sci.* 278 (6) (2000) 532–538, <https://doi.org/10.1007/s003960050551>.
- [45] S. Humbert, O. Lame, R. Séguéla, G. Vigier, A re-examination of the elastic modulus dependence on crystallinity in semi-crystalline polymers, *Polym. (Guildf.)* 52 (21) (2011) 4899–4909, <https://doi.org/10.1016/j.polymer.2011.07.060>.
- [46] A. Morel, S. Domaschke, V. Kumaran, D. Alexeev, A. Sadeghpour, S. Ramakrishna, S. Ferguson, R. Rossi, E. Mazza, A.E. Ehret, G. Fortunato, Correlating diameter, mechanical and structural properties of poly (L-Lactide) fibres from needleless electrospinning, *Acta Biomater.* 81 (2018), <https://doi.org/10.1016/j.actbio.2018.09.055>.
- [47] J.H. Hoh, A. Engel, Friction effects on force measurements with an atomic force microscope, *Langmuir* 9 (11) (1993) 3310–3312.
- [48] L. Sirghi, J. Ponti, F. Broggi, F. Rossi, Probing elasticity and adhesion of live cells by atomic force microscopy indentation, *Eur. Biophys. J.* 37 (6) (2008) 935–945, <https://doi.org/10.1007/s00249-008-0311-2>.
- [49] H. Xue, J. Zhang, S. Han, M. Sun, X. Yan, H. Li, Effect of asphaltene on the structure and surface properties of wax crystals in waxy oils, *Energy Fuels* 33 (10) (2019) 9570–9584, <https://doi.org/10.1021/acs.energyfuels.9b01825>.
- [50] T. Jung, J.-N. Kim, S.-P. Kang, Influence of polymeric additives on paraffin wax crystallization in model oils, *Korean J. Chem. Eng.* 33 (6) (2016) 1813–1822, <https://doi.org/10.1007/s11814-016-0052-3>.
- [51] F. Yang, Y. Zhao, J. Sjöblom, C. Li, K. Paso, Polymeric wax inhibitors and pour point depressants for waxy crude oils: a critical review, *J. Dispers. Sci. Technol.* 36 (2014) 213–225, <https://doi.org/10.1080/01932691.2014.901917>.
- [52] M. Kurniawan, S. Subramanian, J. Norrman, K. Paso, Influence of microcrystalline wax on the properties of model wax-oil gels, *Energy Fuels* 32 (5) (2018) 5857–5867, <https://doi.org/10.1021/acs.energyfuels.8b00774>.